



## Hamster organotypic kidney culture model of early-stage SARS-CoV-2 infection highlights a two-step renal susceptibility

Sophie Shyfrin, Marion Ferren, Laure Perrin-Cocon, Maxime Espi, Xavier Charmetant, Manon Brailly, Didier Decimo, Mathieu Iampietro, Lola Canus, Branka Horvat, et al.

### ► To cite this version:

Sophie Shyfrin, Marion Ferren, Laure Perrin-Cocon, Maxime Espi, Xavier Charmetant, et al.. Hamster organotypic kidney culture model of early-stage SARS-CoV-2 infection highlights a two-step renal susceptibility. *Journal of Tissue Engineering and Regenerative Medicine*, 2022, 13, pp.204173142211221. 10.1177/20417314221122130 . hal-03777088

**HAL Id: hal-03777088**

**<https://cnrs.hal.science/hal-03777088>**

Submitted on 20 Oct 2022

**HAL** is a multi-disciplinary open access archive for the deposit and dissemination of scientific research documents, whether they are published or not. The documents may come from teaching and research institutions in France or abroad, or from public or private research centers.

L'archive ouverte pluridisciplinaire **HAL**, est destinée au dépôt et à la diffusion de documents scientifiques de niveau recherche, publiés ou non, émanant des établissements d'enseignement et de recherche français ou étrangers, des laboratoires publics ou privés.

# Hamster organotypic kidney culture model of early-stage SARS-CoV-2 infection highlights a two-step renal susceptibility

Journal of Tissue Engineering  
Volume 13: 1–15  
© The Author(s) 2022  
Article reuse guidelines:  
sagepub.com/journals-permissions  
DOI: 10.1177/20417314221122130  
journals.sagepub.com/home/tej



Sophie R Shyfrin<sup>1,2</sup>, Marion Ferren<sup>1,2</sup>, Laure Perrin-Cocon<sup>3</sup>,  
Maxime Espi<sup>4</sup>, Xavier Charmetant<sup>4</sup>, Manon Brailly<sup>2</sup>,  
Didier Decimo<sup>1,2</sup>, Mathieu Iampietro<sup>2</sup>, Lola Canus<sup>1</sup>,  
Branka Horvat<sup>2</sup>, Vincent Lotteau<sup>3</sup>, Pierre-Olivier Vidalain<sup>3</sup>,  
Olivier Thaumat<sup>4,5</sup> and Cyrille Mathieu<sup>1,2</sup>

## Abstract

Kidney pathology is frequently reported in patients hospitalized with COVID-19, the pandemic disease caused by the Severe acute respiratory coronavirus 2 (SARS-CoV-2). However, due to a lack of suitable study models, the events occurring in the kidney during the earliest stages of infection remain unknown. We have developed hamster organotypic kidney cultures (OKCs) to study the early stages of direct renal infection. OKCs maintained key renal structures in their native three-dimensional arrangement. SARS-CoV-2 productively replicated in hamster OKCs, initially targeting endothelial cells and later disseminating into proximal tubules. We observed a delayed interferon response, markers of necroptosis and pyroptosis, and an early repression of pro-inflammatory cytokines transcription followed by a strong later upregulation. While it remains an open question whether an active replication of SARS-CoV-2 takes place in the kidneys of COVID-19 patients with AKI, our model provides new insights into the kinetics of SARS-CoV-2 kidney infection and can serve as a powerful tool for studying kidney infection by other pathogens and testing the renal toxicity of drugs.

## Keywords

SARS-CoV-2, kidney, organotypic cultures

Received: 1 May 2022; accepted: 11 August 2022

<sup>1</sup>CIRI, Centre International de Recherche en Infectiologie, Team Neuro-Invasion, TROPism and VIRal Encephalitis, Univ Lyon, Inserm, U1111, CNRS, UMR5308, Université Claude Bernard Lyon 1, Ecole Normale Supérieure de Lyon, Lyon, France

<sup>2</sup>CIRI, Centre International de Recherche en Infectiologie, Team Immunobiology of the Viral infections, Univ Lyon, Inserm, U1111, CNRS, UMR5308, Université Claude Bernard Lyon 1, Ecole Normale Supérieure de Lyon, Lyon, France

<sup>3</sup>CIRI, Centre International de Recherche en Infectiologie, Team Viral Infection, Metabolism and Immunity, Univ Lyon, Inserm, U1111, CNRS, UMR5308, Université Claude Bernard Lyon 1, Ecole Normale Supérieure de Lyon, Lyon, France

<sup>4</sup>CIRI, Centre International de Recherche en Infectiologie, Team Normal and pathogenic B cell responses, Univ Lyon, Inserm, U1111, CNRS, UMR5308, Université Claude Bernard Lyon 1, Ecole Normale Supérieure de Lyon, Lyon, France

<sup>5</sup>Hospices Civils de Lyon, Edouard Herriot Hospital, Department of Transplantation, Nephrology and Clinical Immunology, Lyon, France

## Corresponding author:

Cyrille Mathieu, CIRI, Centre International de Recherche en Infectiologie, Team Neuro-Invasion, TROPism and VIRal Encephalitis, Univ Lyon, Inserm, U1111, CNRS, UMR5308, Université Claude Bernard Lyon 1, Ecole Normale Supérieure de Lyon, 21 avenue Tony Garnier, Tour CERVI, Lyon 69364, France.  
Email: cyrille.mathieu@inserm.fr



## Introduction

Severe acute respiratory syndrome coronavirus 2 (SARS-CoV-2) is the causative agent of Coronavirus Disease 2019 (COVID-19),<sup>1</sup> a pandemic disease that in January 2022 has counted at least 454.5 million cases and claimed 6 million lives worldwide,<sup>2</sup> leading to devastating personal, social, and economic consequences. Pulmonary failure is the most common symptom of severe COVID-19. However, COVID-19 can also involve cardiovascular, neurological, gastrointestinal, hepatic and renal complications potentially resulting in multiorgan failure.<sup>3</sup> While being rare in the mild and moderate form of the disease, acute kidney injury (AKI) is frequently reported in hospitalized patients, reaching 50% for patients in critical care units. In such cases, AKI is a significant predictor of poor outcome.<sup>4–10</sup> Furthermore, a persistent decline in renal function has been documented in discharged COVID-19 patients, including a proportion of those not presenting with AKI during the acute phase of the disease, for at least 6 months of follow-up.<sup>11</sup> An increased risk of AKI and chronic kidney disease development in post-acute COVID-19 has also been reported.<sup>12</sup> As long-term COVID-19 sequelae affect millions of recovered patients, such complications may become a significant public health concern.<sup>13,14</sup>

Studies of kidney autopsy samples from COVID-19 patients with AKI reveal signs of acute tubular necrosis, collapsing glomerulopathy and thrombotic microangiopathy. Knowledge of the precise mechanisms underlying renal pathology in acute and post-acute COVID-19 remain scarce.<sup>5,7,15</sup> AKI could be a consequence of microangiopathy, thrombosis, rhabdomyolysis, inflammatory cytokine expression and complement activation. It may also be related to ventilation-induced alterations in blood flow, hemodynamic failure and to the nephrotoxicity of drugs used to treat the patients. Moreover, SARS-CoV-2 particles have been detected in renal biopsies, suggesting direct infection and viral replication may cause cytopathic effects in the kidney.<sup>9,16–22</sup> Further investigation is required to confirm whether the virus can replicate in renal tissue, identify its initial cellular targets and dissemination pattern, and elucidate the organ's response to infection.

To date, the vast majority of samples used to study renal involvement in COVID-19 were obtained via autopsy or biopsy from patients with advanced disease, and do not provide information regarding the early stages of renal infection.<sup>7</sup> As in the case of other nephrotropic pathogens, studying SARS-CoV-2 kidney infection is challenging due to the lack of relevant *in vitro* models and the difficulties in monitoring an *in vivo* infection in a non-invasive way.<sup>23,24</sup> In order to gain insight into the early stages of SARS-CoV-2 infection of kidney, we turned to organotypic culture systems. In this *ex vivo* model, 350–500  $\mu\text{m}$  thick slices of organs are cultured on an air-liquid interface. Organotypic cultures represent the only model

containing all cell types from an organ of interest in their native three-dimensional arrangement.<sup>25,26</sup> Organotypic cultures prepared from mouse and hamster brain have been used successfully to study the infection of the central nervous system by Measles virus<sup>26</sup> and Nipah virus,<sup>27</sup> or, together with lung organotypic cultures, by SARS-CoV-2.<sup>25</sup> Organotypic cultures from human and mouse kidney slices have been described previously but have never been used to study SARS-CoV-2 or other viral infections.<sup>28–31</sup>

Live samples of human kidneys are very difficult to obtain for obvious ethical reasons. Golden Syrian hamsters (*Mesocricetus auratus*) are a representative and economical model for SARS-CoV-2 infection. When challenged with SARS-CoV-2, they develop symptoms mimicking mild disease in humans and accumulate a viral load in various organs, including kidney.<sup>32</sup> Recently, our group has developed and characterized hamster organotypic lung, brainstem and cerebellum cultures as models for studying SARS-CoV-2 infection and platforms for testing antiviral drugs.<sup>25</sup> To study SARS-CoV-2 infection in renal tissue, we have now developed hamster organotypic kidney cultures (OKCs). SARS-CoV-2 infection of these organotypic cultures was effective, thus supporting the possibility of active viral replication in human kidneys. Our OKC models proved particularly valuable for investigating the tropism and dissemination of SARS-CoV-2 in renal tissue and analyzing its innate immune response to infection.

## Materials and methods

**Animals and ethical authorization.** Syrian golden hamsters (*Mesocricetus auratus*) used in this study were obtained from Janvier Labs (Le Genest-Saint-Isle, France) with clean health monitoring report. K18-hACE2 mice were obtained from the Jackson laboratory. The sex of the animals was random and dependent on the litter throw by the mother. Animals were euthanized at 7 days old. This study was performed according to French ethical committee (CECCAPP) regulations (accreditation CECCAPP\_ENS\_2014\_034).

**Preparation of organotypic cultures.** The procedure for Organotypic Kidney Cultures (OKC) was adapted from the protocol for Organotypic Brain Cultures (OBC) described previously.<sup>33</sup> A day before the dissection, Millicell® cell culture inserts with PTFE membranes (Merck) were pre-activated with OKC medium. The OKC medium contains 375 mL of Minimal Essential Medium GlutaMAX (ThermoFisher Scientific), 125 mL of heat-inactivated horse serum (Gibco), 2.5 g of D-glucose (Sigma-Aldrich) and 1 mL of human recombinant insulin (10 mg/mL) (Sigma-Aldrich), and was sterilized with a 0.22  $\mu\text{m}$  filter. The OKC medium is identical to the OBC medium described by Welsch<sup>33</sup> and used by Ferren et al.<sup>25</sup> for organotypic lung,

brainstem and cerebellum cultures. Seven to nine-day suckling hamsters were sacrificed and their abdominal cavity was opened. Kidneys were collected and placed into a solution of Hibernate<sup>®</sup>-A medium (Sigma-Aldrich), 1X kynurenic acid solution (for a 10X solution: 378 mg of kynurenic acid (Sigma-Aldrich) in 170 mL of H<sub>2</sub>O, 20 mL of 1 M MgCl<sub>2</sub> (Sigma-Aldrich) adjusted to pH 7.4 with 0.1 M NaOH (Sigma-Aldrich), 1 mL HEPES (Sigma-Aldrich), adjusted to a final volume of 200 mL) and 1X penicillin/streptomycin solution (Corning). Kidneys were placed on six layers of Whatman paper with their longitudinal axis perpendicular to the tissue chopper blade and sliced transversely using the McIlwain<sup>®</sup> tissue chopper (Campden Instruments) at 500  $\mu$ m thickness for all experiments except the Seahorse XF Analyzer Respiratory Assay that required 400  $\mu$ m slices. The slices were dissociated under a dissection microscope. Undamaged and homogenous slices were selected and maintained on an air-liquid interface provided by PTFE membranes pre-activated with OKC medium. Organotypic lung cultures were prepared using the protocol described by Ferren et al.<sup>25</sup>

**Viruses and infection of organotypic kidney cultures.** Viral stocks have been produced and titrated at 37°C in Vero E6 cells. Briefly, cells were infected at a Multiplicity Of Infection (MOI) of 0.01 in DMEM. After 90 min of incubation at 37°C, the medium was replaced with DMEM-2% FBS and the cells were incubated at 37°C in 5% CO<sub>2</sub> atmosphere for 2 days. Viral supernatants were collected and centrifuged (400  $\times$  g, 5 min), aliquoted, and titrated as plaque-forming units using a classic dilution limit assay. A 2  $\mu$ L drop containing the required amount of viral plaque-forming units (pfu) was placed on each organotypic kidney slice. Infected slices were incubated at 37°C until collection. Slices were infected with wild-type SARS-CoV-2 (2019-nCoV/USA\_WA1/2020) or a recombinant strain icSARS-CoV-2-mNG expressing the mNeonGreen reporter gene inserted into its ORF7.<sup>34</sup>

**Seahorse XF analyzer respiratory assay.** Organotypic kidney slices were prepared and sliced in Neurobasal<sup>®</sup>-A Medium 1X (Gibco) at 400  $\mu$ m and assayed on the day of preparation (day 0) or following 1 or 4 days of culture at air-liquid interface with OKC medium at 37°C. OKCs were washed in 1X phosphate buffer saline (Gibco). 1 mm punches were prepared from the renal cortex and 1 punch/well was placed in a 24-wells islet capture microplate (Agilent). Punches were washed twice with 1 mL Seahorse XF DMEM medium (pH 7.4) supplemented with glucose (10 mM), pyruvate (1 mM) and L-glutamine (2 mM) and incubated 1 h at 37°C in a non-CO<sub>2</sub> incubator. 500  $\mu$ L of fresh Seahorse medium were added to each well before the respiration assay. The oxygen consumption rate (OCR) was measured using the MitoStress test (Agilent), optimized for tissue assay according to the method described

by Underwood et al.<sup>35</sup> Seahorse running program: injection Port A—3  $\mu$ M Oligomycin; Injection Port B—3  $\mu$ M FCCP with 0.7 mM Pyruvate and injection Port C—6  $\mu$ M Rotenone and 6  $\mu$ M Antimycin A. Results were analyzed using the Seahorse Wave software.

**Quantitative RT-PCR.** Each organotypic kidney slice was collected in 350  $\mu$ L of RA1 buffer (NucleoSpin RNA, Macherey-Nagel) and 3.5  $\mu$ L of 2-Mercaptoethanol (Sigma-Aldrich), and lysed using a pestle mixer (Argos Technologies). RNA was extracted from the lysates with the NucleoSpin RNA kit (Macherey-Nagel). 200 ng of RNA was reverse transcribed with the iScript cDNA Synthesis Kit (Bio-Rad) according to the manufacturers' protocols. cDNA was diluted 1:10 to avoid inhibition between mix with the following step. Gene transcription was quantified via qPCR using the Platinum SYBR Green qPCR SuperMix-UDG (Invitrogen), according to the manufacturer's protocol. Readings were made with the StepOne-Plus Quantitative PCR System (Applied Biosystems) and viewed in the StepOne version 2.3 software (Applied Biosystems). The primers for measuring the expression of the mRNA of the cytokines IL-4, IL-10, IL-13, and IL-22 were designed for this study (Supplemental Table 1). Other primers were designed by Ferren et al.<sup>25</sup> The efficacy (*E*) of the primers was calculated as  $10^{-1/\text{slope}}$  based on the slope of the standard curve. The copy number of mRNA per  $\mu$ g of total RNA was calculated using the  $E^{-\Delta\Delta CT}$  model<sup>36</sup> (for each gene and normalized by the standard deviation in the expression of glyceraldehyde-3-phosphate dehydrogenase (GAPDH), a housekeeping gene (UniProtKB P04406), from the mean of its expression level across all days.<sup>37</sup>

**Immunofluorescence staining.** Organotypic kidney slices were fixed overnight at 4°C in 4% paraformaldehyde (16% paraformaldehyde, methanol-free; ThermoFisher Scientific) diluted in phosphate buffer saline (PBS 1X; Gibco). Slices were washed with PBS 1X (here and later: 4 times, 5 min each wash) and placed into a sucrose (Sigma-Aldrich) gradient (5%, 15%, 20%) solution overnight at 4°C. Slices were embedded in the Optimal Cutting Temperature (OCT) solution (ThermoFisher Scientific) and sectioned along the horizontal plane with the Leica CM3050 S cryostat-microtome (Leica Biosystems). 10  $\mu$ m sections were placed on Superfrost Gold Plus adhesion slides (Fisher Scientific), washed in PBS 1X, permeabilized and blocked in permeabilization and blocking solution (1X DPBS; ThermoFisher Scientific, 3% BSA; Sigma-Aldrich, 0.3% Triton-X100; Sigma-Aldrich) for 30 min at 4°C. Slices were incubated overnight with primary antibodies diluted in permeabilization and blocking solution, washed in PBS 1X, stained for 1 h with secondary antibodies diluted in permeabilization and blocking solution, washed with PBS 1X and mounted in Fluoromount-G<sup>®</sup> aqueous mounting medium (SouthernBiotech).



Anti-SARS-CoV-2 nucleoprotein (NP) antibodies (SinoBiological, Cat# 40143-MM05 mouse, 1:200 dilution) were used to detect the presence of virus. Endothelial cells were stained with anti-CD34 antibodies (abcam, Cat# ab81289 rabbit, 1:100 dilution), proximal tubular epithelial cells with anti-aquaporin-1 (ThermoFisher Scientific, Cat# PA5-53954 rabbit, 1:100 dilution), and podocytes with anti-nephrin (abcam, Cat# ab216341, rabbit, 1:100 dilution). Alexa FluorTM 488 donkey anti-rabbit (ThermoFisher Scientific, Cat# A21206, 1:500 dilution) and Alexa FluorTM 555 donkey anti-mouse (ThermoFisher Scientific, Cat# A31570, 1:500 dilution) secondary antibodies were used. Cell nuclei were stained with 4',6-diamidino-2-phenylindole (DAPI) (ThermoFisher Scientific, Cat# 62248, 1:1000 dilution).

**Imaging.** OKCs infected with icSARS-CoV-2-mNG were photographed using the Nikon Eclipse Ts2R optical microscope and stitched using the Stitching plugin in ImageJ.<sup>38</sup> Immunostained OKCs were examined and photographed using the Zeiss Axio Observer.Z1 microscope with confocal unit LSM 980 (Zeiss). Images were edited and analyzed using the ImageJ software 1.52p FiJi package<sup>39</sup> and assembled in Inkscape.

**Statistical analysis.** Statistical analysis was performed in GraphPad Prism version 9.3.0.<sup>40</sup> For the Seahorse XF metabolic activity assay, day 1 and day 4 OCRs of punches were compared to the day 0 OCR using ordinary one-way ANOVA. For the gene expression analysis, differences between normalized mRNA copy numbers per  $\mu\text{g}$  RNA in infected and non-infected samples were compared using a Mann-Whitney U-test.  $*=p<0.05$ ;  $**=p<0.01$ ;  $***=p<0.001$ .

## Results

### *Organotypic kidney cultures maintain key renal native structures for at least 4 days in culture*

Kidneys were collected from 7-day-old suckling hamsters, sliced on a tissue chopper into 500  $\mu\text{m}$  thick slices and maintained on an air-liquid interface provided by polytetrafluoroethylene membranes. The renal capsule, cortex and medulla were clearly identifiable in hamster OKCs (Figure 1(a)). A nephron (Figure 1(b)) is a functional unit of the kidney. Blood is filtered in the renal glomerulus (Figure 1(c)). Through the afferent arteriole, it enters under high pressure a capillary bundle known as the glomerulus and passes the filtration barrier consisting of the glomerular endothelium, basement membrane and podocytes. The filtration barrier retains blood cells, large particles and proteins but not nutrients or ions. Glucose, amino acids, water and salts are re-absorbed into capillaries from the filtrate in the proximal convoluted tubule, loop of Henle and distal convoluted tubule. Following reabsorption, the filtrate becomes urine and flows into the collecting duct

leading to the renal pelvis and, eventually, the ureter.<sup>41</sup> We confirmed the presence of essential functional elements of nephrons in our OKCs via immunofluorescence staining of aquaporin-positive proximal tubules, nephrin-positive podocytes and CD34-positive endothelial cells of the renal vasculature. Reflecting their native arrangement, proximal tubules and renal glomeruli were localized in the cortex (Figure 1(d)). However, we then further determined whether organotypic kidney slices survive in culture and maintain metabolic activity for up to 4 days after preparation. To measure the mitochondrial respiratory activity of OKCs, 1 mm large punches prepared from the cortical zone of 400  $\mu\text{m}$ -thick slices were analyzed on a Seahorse XF Analyzer using the MitoStress Test with procedures adapted for tissue.<sup>35</sup> Oxygen Consumption Rate (OCR) was monitored at basal stage and after addition of mitochondrial modulators to determine the basal and maximal respiratory capacity of OKCs. The maximal metabolic rate was monitored following disruption of the mitochondrial proton gradient by FCCP. Non-mitochondrial OCR measured after complete inhibition of mitochondrial respiration by rotenone and antimycin A was subtracted to basal and maximal OCR to calculate basal and maximal respiration (Figure 2(a)). The basal metabolic activity of punches from OKC cortices was maintained after 1 day of culture and remained at more than 60% of its initial level on day 4 (Figure 2(a) and (b)). As shown in Figure 2(c), maximal respiration remained stable after 1 day of culture and decreased by only 20% at day 4. According to the immunofluorescent staining, the arrangement of the OKC structure was preserved even after 4 days of culture (Figure 3(d) and (e)).

Total RNA was extracted from slices and quantified as another measure of their viability. Over the duration of the experiment, its amount did not decrease (Figure 2(d)). The expression of glyceraldehyde-3-phosphate dehydrogenase (GAPDH), a key enzyme in the glycolysis pathway and a housekeeping gene (UniProtKB P04406), also remained stable (Figure 2(e)), reflecting the ability of OKCs to maintain steady glycolytic activity in culture. Such results indicate that, despite a progressive reduction in mitochondrial respiration, organotypic kidney cultures remain viable on an air-liquid interface for at least 4 days.

### *Organotypic kidney cultures are highly permissive to SARS-CoV-2 infection*

SARS-CoV-2 mainly enters cells via the binding of the Spike glycoprotein to one of its target receptors such as angiotensin converting enzyme 2 (ACE2) or Neuropilin-1. The fusion of the viral envelope with the cell membrane is enhanced by the cleavage of the Spike by host proteases such as TMPRSS2 on the cell surface or cathepsins B and L in endosomes.<sup>42,43</sup> These proteins are all expressed in the kidney,<sup>44</sup> especially ACE2 which is critically involved in

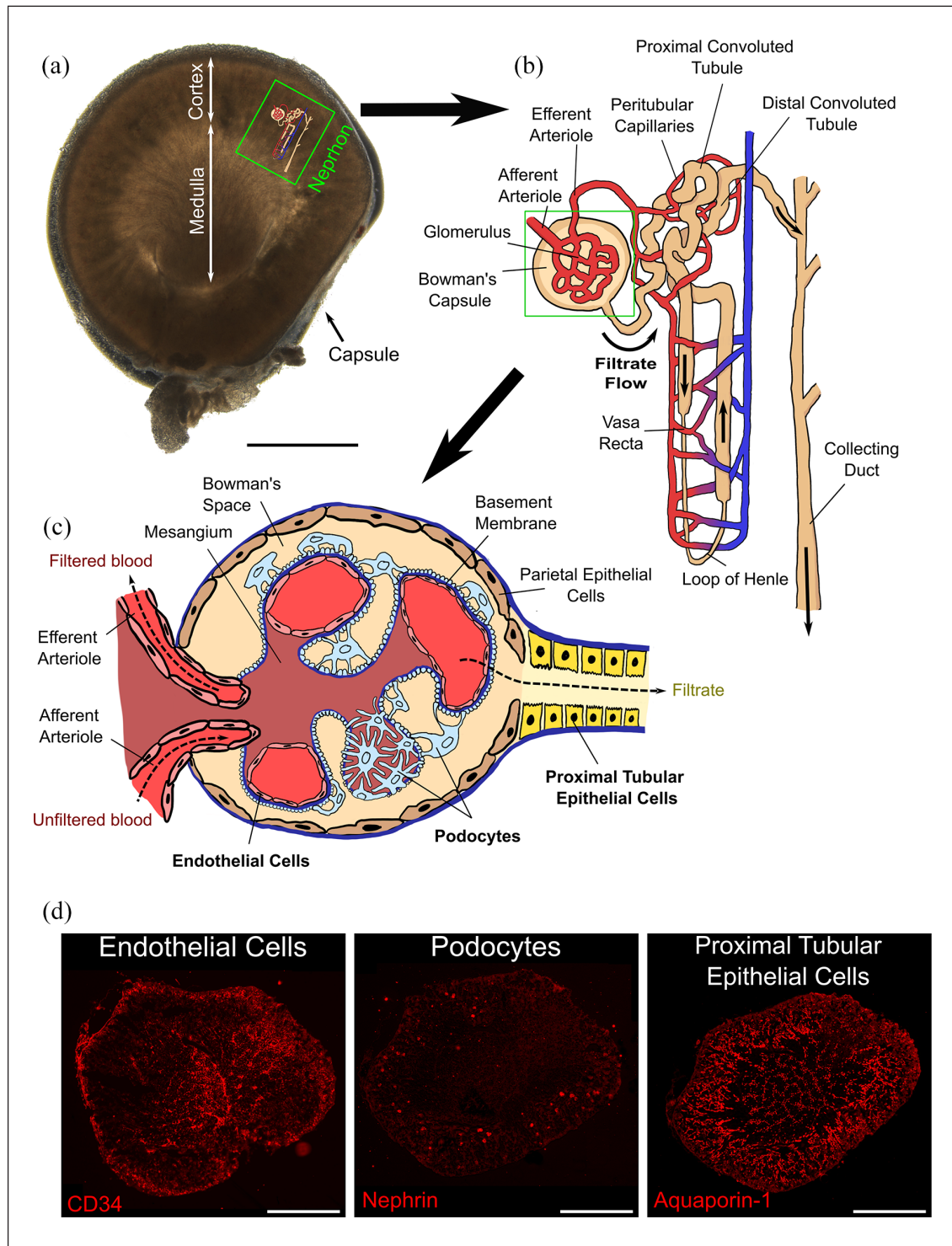


**Figure 1.** Schematic representation of the anatomy of hamster organotypic kidney cultures. (a) A 500- $\mu$ m thick organotypic kidney slice maintained on an air-liquid interface provided by a PTFE membrane was photographed in brightfield using a Nikon Eclipse Ts2R epifluorescence microscope. Scalebar = 1 mm. The renal capsule, cortex and medulla are identified and labeled. A nephron is positioned in its physiological location and highlighted with a green rectangle. (b) The structure of a nephron, a functional unit of the kidney, showing the flow of the filtrate. (c) The structure of a renal corpuscle. The schematic was rendered in-house using Procreate® and Inkscape I.I. (d) Organotypic kidney cultures were fixed in 4% paraformaldehyde, embedded in OCT solution and cryosectioned at 10  $\mu$ m thickness. Sections were immunostained to visualize endothelial cells, podocytes and proximal tubular epithelial cells with anti-CD34 (endothelial cells; left panel), anti-nephrin (podocytes; middle panel) and anti-aquaporin I (proximal tubular epithelial cells) primary antibodies (right panel). Scalebar = 1 mm. Images were reconstructed using the Stitching plugin in ImageJ.<sup>38</sup>

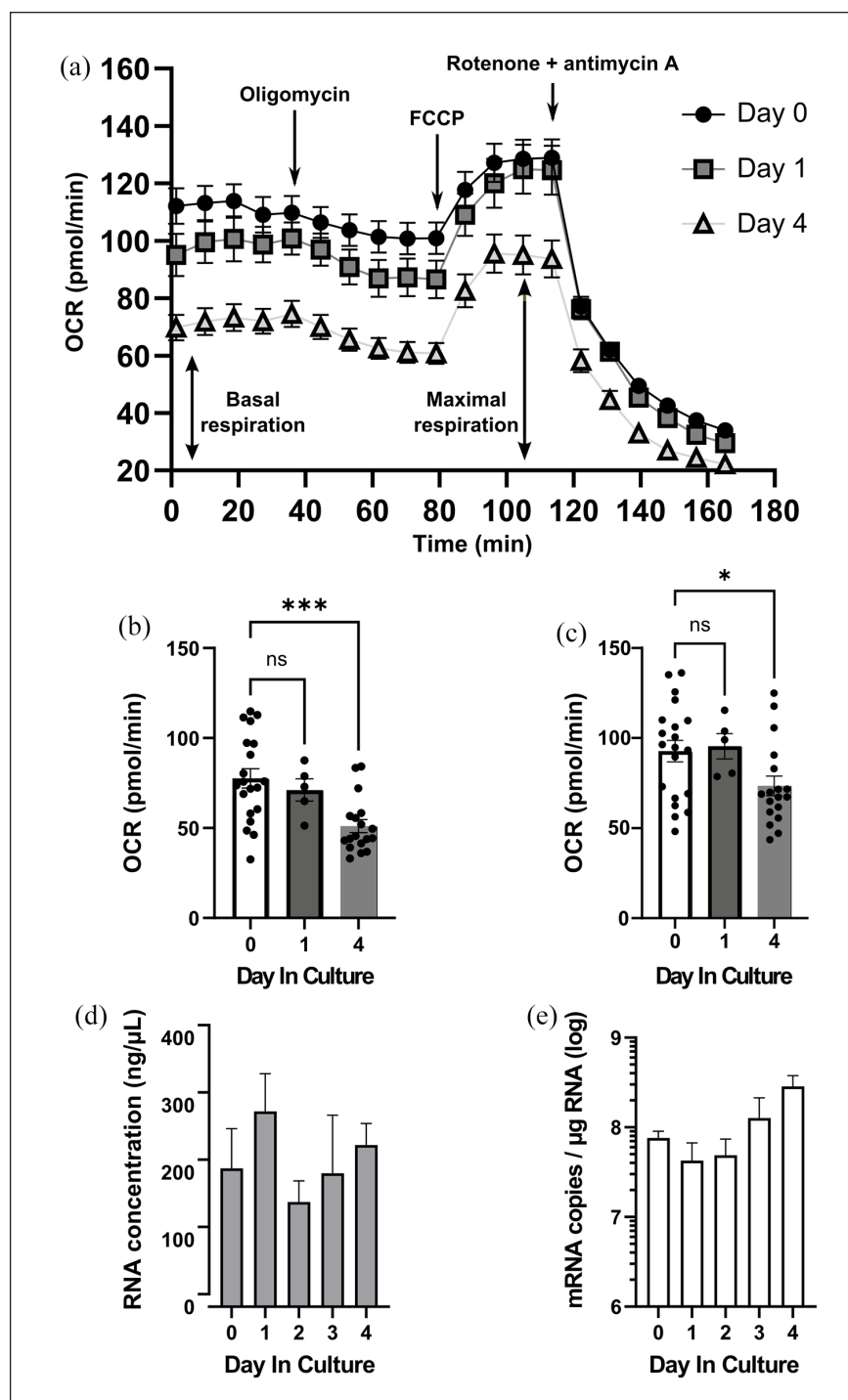


**Figure 2.** Viability of hamster organotypic slices in culture. The Seahorse XF Analyzer was used to analyze the metabolic activity of OKCs. Briefly, 400- $\mu$ m thick OKCs were maintained at an air-liquid interface in the OKC medium for 0, 1 or 4 days prior to measurement. One punch per slice was cut in the cortical zone and basal and maximal respiration of each punch was determined using the MitoStress test. The oxygen consumption rate (OCR) was measured according to time. Punches received successive additions of respiratory modulators indicated by arrows, ATP synthase inhibitor oligomycin (3  $\mu$ M), uncoupling agent FCCP (3  $\mu$ M) with pyruvate supplement (0.7 mM), and then rotenone + antimycin A (6  $\mu$ M) to completely inhibited mitochondrial respiration. (a) For each experiment, mean OCR  $\pm$  SEM is plotted. Determination of the basal and maximal respiration is indicated with green arrows on the mean OCR curve obtained at day 4. (b) Basal and (c) maximal respiration rates of OKCs. Mean respiration rates obtained at day 1 and 4 were compared to that of day 0 using ordinary one-way ANOVA. \*,  $p < 0.05$ ; \*\*,  $p < 0.01$ ; \*\*\*,  $p < 0.001$ . (d) Concentration of RNA extracted from non-infected OKCs collected after 0 to 4 days of culture. (e) Expression of GAPDH in non-infected OKCs collected after 0 to 4 days of culture.

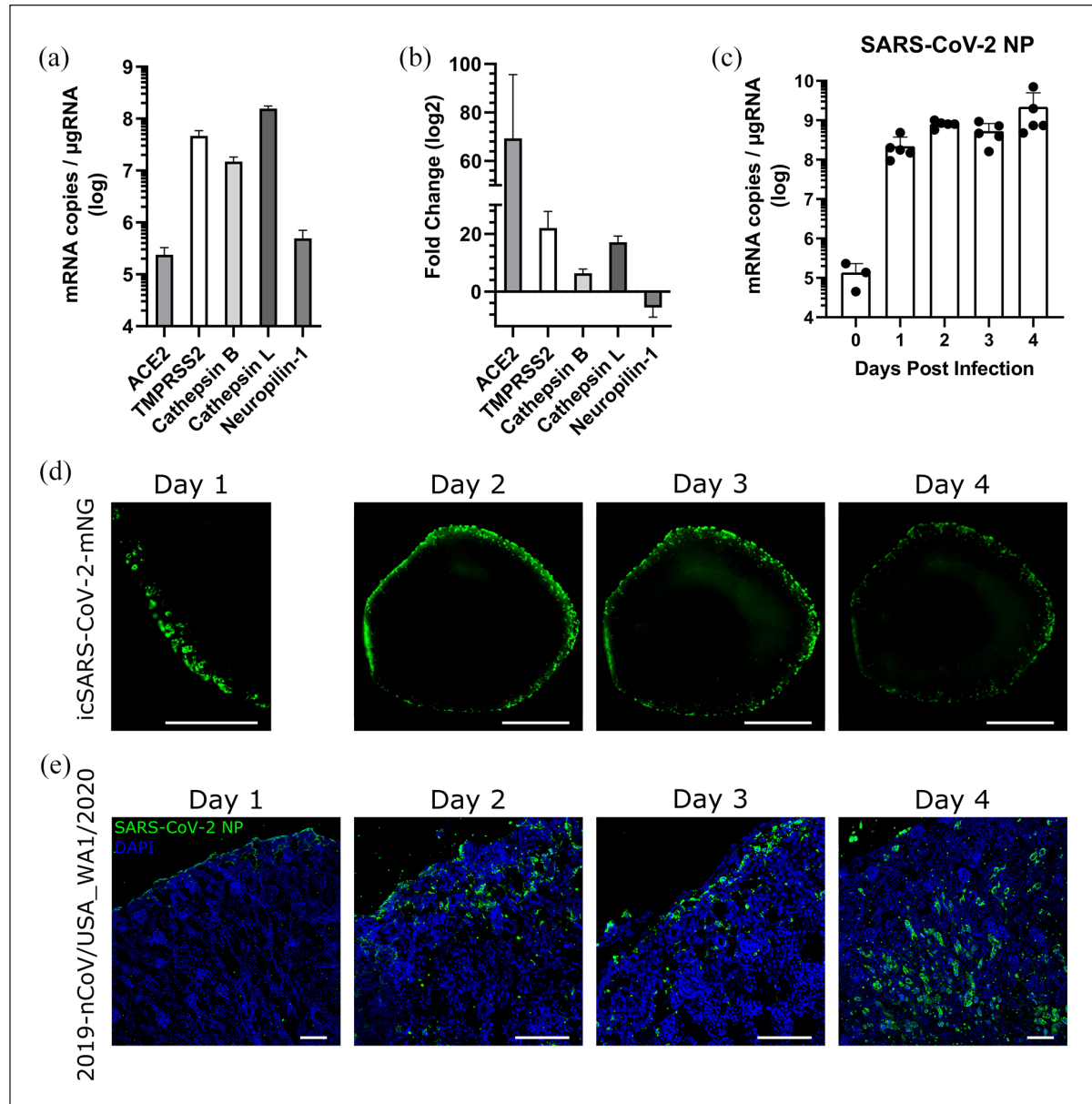


**Figure 3.** SARS-CoV-2 permissiveness of and progression in hamster organotypic kidney cultures. (a and b) Gene expression was quantified in non-infected organotypic kidney cultures (OKCs) and hamster organotypic lung cultures collected on the day of dissection via RT-qPCR as the number of mRNA copies per  $\mu\text{g}$  of total RNA and normalized by the standard deviation in GAPDH expression. (a) mRNA copy numbers of candidate SARS-CoV-2 entry factors per  $\mu\text{g}$  of total RNA. (b) Fold change of SARS-CoV-2 entry factor mRNA copy numbers per  $\mu\text{g}$  of total RNA in OKCs compared to organotypic lung cultures. (c) Hamster organotypic cultures were infected with 1000 pfu of wild-type SARS-CoV-2 (2019-nCoV/USA\_WA1/2020) and collected every day from day 0 (90 min post-infection) to day 4 post-infection. SARS-CoV-2 replication was measured by quantifying the amount of SARS-CoV-2 nucleocapsid (NP) mRNA per  $\mu\text{g}$  of total mRNA via RT-qPCR and normalizing it by the expression of a housekeeping gene (GAPDH). (d) Hamster OKCs infected with 10,000 pfu of SARS-CoV-2\_mNeon Green (icSARS-CoV-2-mNG) were imaged from day 0 to day 4 post-infection using a Nikon Eclipse Ts2R epifluorescence microscope. Scalebar = 1 mm. (e) Hamster OKCs were infected with 1000 pfu of wild-type SARS-CoV-2 and fixed in 4% paraformaldehyde every day from 1 to 4 days post infection. OKC sections were stained against SARS-CoV-2 nucleoprotein (NP). Cell nuclei were stained with 4',6-diamidino-2-phenylindole (DAPI). Pictures were obtained by confocal microscopy. Scalebar = 100  $\mu\text{m}$ .

the renin-angiotensin system responsible for controlling blood pressure and vascular resistance.<sup>45,46</sup> The global expression of SARS-CoV-2 entry factors in hamster OKCs

was quantified via RT-qPCR. The entry receptors ACE2 and neuropilin-1, as well as the proteases TMPRSS2 and cathepsins B and L were highly expressed in the slices



(Figure 3(a)). The mRNA expression of all entry factors except neuropilin-1 was significantly enriched compared to lung organotypic cultures (Figure 3(b)).

In order to probe the susceptibility of hamster OKCs to SARS-CoV-2, five slices from five animals ( $n=5$ ) were infected with wild-type SARS-CoV-2 (2019-nCoV/USA\_WA1/2020) while maintained in culture on an air-liquid interface. The number of copies of mRNA encoding the viral nucleocapsid protein (NP) was quantified via RT-qPCR in slices from day 0 to day 4 post-infection, starting 90 min post-infection. Similarly to the pattern observed in hamster organotypic lung cultures,<sup>25</sup> viral mRNA expression increased by four logs in infected OKCs, approaching a plateau at 1 day post-infection (Figure 3(c)). In slices infected with a recombinant SARS-CoV-2 strain encoding a mNeonGreen reporter (icSARS-CoV-2-mNG), infected cells were observable from day 1 post-infection, thus mirroring the RT-qPCR data (Figure 3(d)). Infection started in the capsular zone (Figure 3(d) and (e)) and propagated toward the center of the slice when using the wild-type virus expressing ORF7 (Figure 3(d) and (e)). Indeed, ORF7 is a known virulence factor that promotes viral growth by controlling the innate antiviral response. The fact that the infection starts in the capsular zone is unexpected. However, the same phenomenon was observed when infecting OKCs from K18-hACE2 mice, which express the entry receptor ubiquitously, with 500 pfu of icSARS-CoV-2-mNG (Supplemental Figure S1). This suggests that SARS-CoV-2 preferentially infects and replicates cells in the capsular zone independently of the expression of the entry receptor. In parallel, we infected the OKCs with a pan-tropic Vesicular Stomatitis Virus expressing GFP (VSV-GFP) (Supplemental Figures S1 and S2). As opposed to icSARS-CoV-2-mNG, VSV extensively infected the medullar area of the cultures from day 1 post-infection. We have also confirmed that the infection of the OKC was productive by plaque assay with the production of pfu peaking 2 days after infection both in the cultures and the culture medium (Supplemental Figure S1C).

### ***In hamster organotypic kidney cultures, SARS-CoV-2 targets endothelial cells and proximal tubules but not podocytes***

To investigate the early tropism and subsequent propagation of SARS-CoV-2 in hamster OKCs further, cells serving as the primary targets of the virus were identified via immunofluorescence. 10  $\mu$ m thick cryosections of OKCs were stained with antibodies against the SARS-CoV-2 nucleoprotein (NP) and markers of endothelial cells (CD34), proximal tubular epithelial cells (aquaporin-1) and podocytes (nephrin) (Figure 4, Supplemental Figures S3 and S4).

In line with observations of slices infected with icSARS-CoV-2-mNG, infection initiated in the subcapsular zone

(Figure 4(a)) and propagated toward the center of the slice (Figure 4(b)). Colocalization of CD34 and SARS-CoV-2 NP was observed on day 1 (Figure 4(a)) and day 2 (Figure S4A) post-infection. At later timepoints, colocalization with CD34<sup>+</sup> cells was restricted to peripheral blood vessels (Supplemental Figures S4A and S4B) and was limited compared to day 1 (Figure 4(a)). Infection of podocytes was not detected over the 4 days of the experiment (Supplemental Figure S3). Proximal tubular epithelial cells positive for viral nucleoprotein were observed on day 4 post-infection (Figure 4(c)), but not at earlier timepoints (Supplemental Figure S4B). These results suggest that early targets of SARS-CoV-2 in hamster OKCs include CD34<sup>+</sup> endothelial cells and other subcapsular parietal cells, while proximal tubular epithelial cells serve as later sites of viral dissemination.

### ***Gene expression analysis of organotypic kidney cultures infected with SARS-CoV-2***

In order to evaluate how organotypic kidney cultures respond to infection, the expression of immune-related genes was measured and compared in infected and non-infected OKCs. No substructures of the OKCs were isolated and entire slices were compared. In particular, we measured the expression of inflammatory cytokines genes (IL-6, IL-1 $\beta$ , IL-18, TNF $\alpha$ ), selected genes associated with highly inflammatory types of programmed cell death (MLKL and gasdermin D), and interferon-stimulated genes that hallmark the antiviral response (CXCL10, MX1). We also monitored the expression of SARS-CoV-2 receptor ACE2 and the entry-associated protease TMPRSS2.

Infected OKCs display a limited expression of TNF $\alpha$  and a repression of IL-1 $\beta$  (Figure 5(a) and (b)), IL-18 (Figure 5(c)), and IL-6 (Figure 5(d)) on days 1 and 2 post-infection, followed by strong induction from day 3 onward, preceding closely the infection of proximal tubular epithelial cells shown in Figure 4(c). This effect was particularly pronounced for IL-1 $\beta$  (Figure 5(b)), which was upregulated approximately 2500-fold between day 2 and 3 post-infection. Although TNF $\alpha$  (Figure 5(a)) was not particularly repressed initially, it displayed a statistically significant upregulation only on day 4. The expression of IL-1 $\beta$  dropped dramatically on day 4, reaching levels equivalent to those of non-infected samples, while the expression of IL-18 and IL-6 was maintained. Necroptosis and pyroptosis are highly inflammatory cell death programs which play a role in the innate antiviral response in parallel to immune mediators.<sup>47</sup> Moreover, cytokines such as TNF $\alpha$  and members of the IL-1 family have been demonstrated to regulate necroptosis and pyroptosis, respectively.<sup>48,49</sup> An upregulation of mixed lineage kinase domain-like pseudokinase (MLKL), a marker of necroptosis, was observed at day 4 post-infection in OKCs, suggesting that necroptosis had

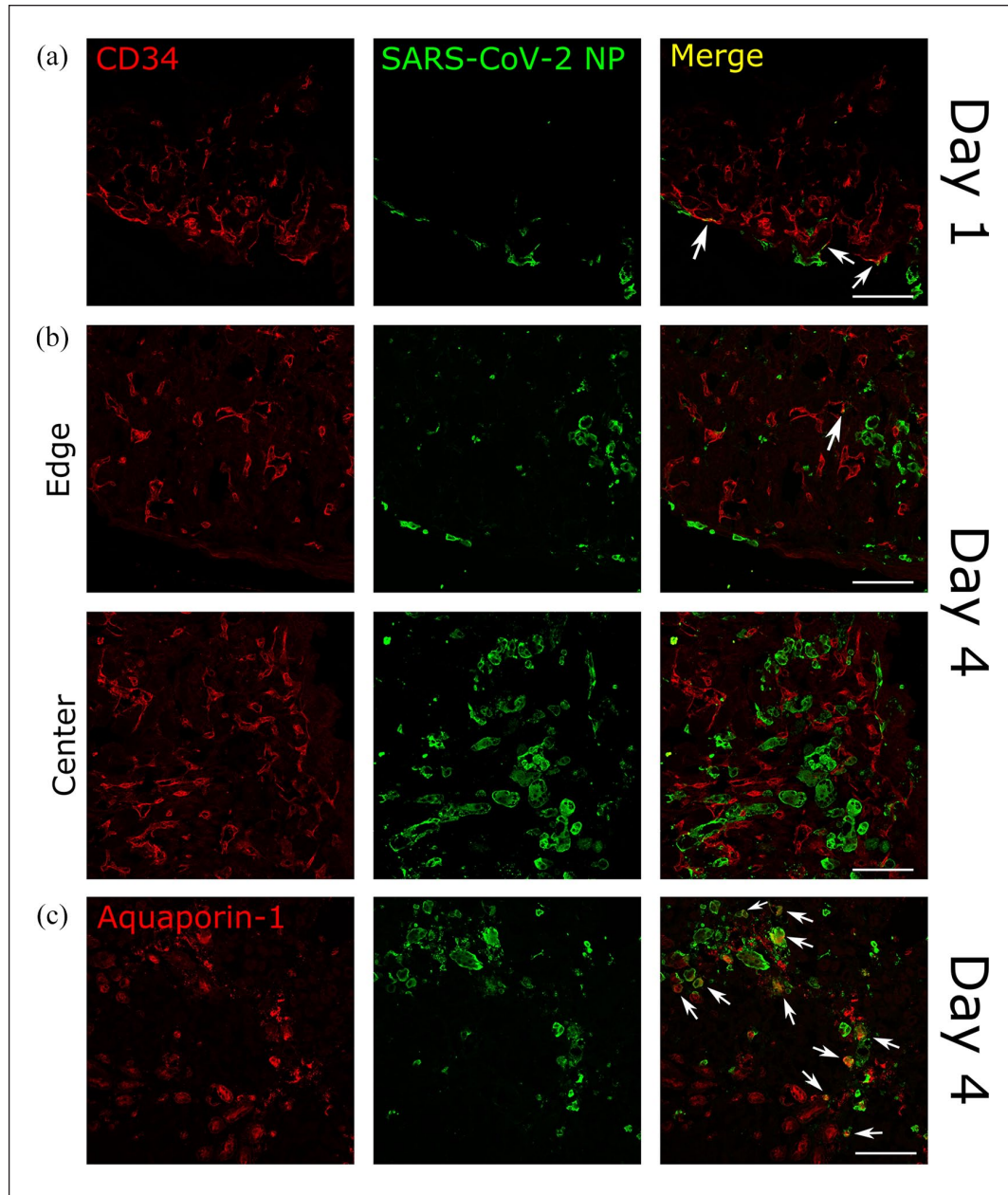


**Figure 4.** Tropism and dissemination of SARS-CoV-2 in hamster organotypic kidney cultures. Organotypic kidney cultures (OKC) were infected with 1000 pfu of wild-type SARS-CoV-2 and fixed in 4% paraformaldehyde at 1 or 4 days post infection (dpi). (a and b) OKC sections stained against SARS-CoV-2 nucleoprotein (NP) and CD34 (marker of endothelial cells) at day 1 and 4 post infection ((a and b), respectively). (a) is showing the edge of the slice. (b) is showing both the edge and the center of the slice, demonstrating the spread of infection toward the center. (c) OKC sections stained against SARS-CoV-2 NP and (c) aquaporin-1 (marker of proximal tubular epithelial cells). Immunofluorescence images were acquired using confocal microscopy and is representative of three independent experiments. Colocalization of cell type markers (red) with SARS-CoV-2 NP (green) is denoted with arrows. Scalebar = 100 μm.

likely been induced at this stage of infection (Figure 5(e)). The expression of gasdermin D, a key mediator of pyroptosis, was raised throughout the experiment, peaking at day 2 post-infection (Figure 5(f)).

The expression of ISGs such as CXCL10 (Figure 5(g)) of the chemokine family and myxovirus resistance 1

(MX1) (Figure 5(h)) were measured as a proxy for an efficient IFN response to SARS-CoV-2 challenge. CXCL10 expression was only induced on day 4, whereas MX1 expression increased 13-fold on day 2 post-infection and continued to rise up to day 4, reaching a 24-fold level compared to non-infected cultures. Thus, it mirrored the

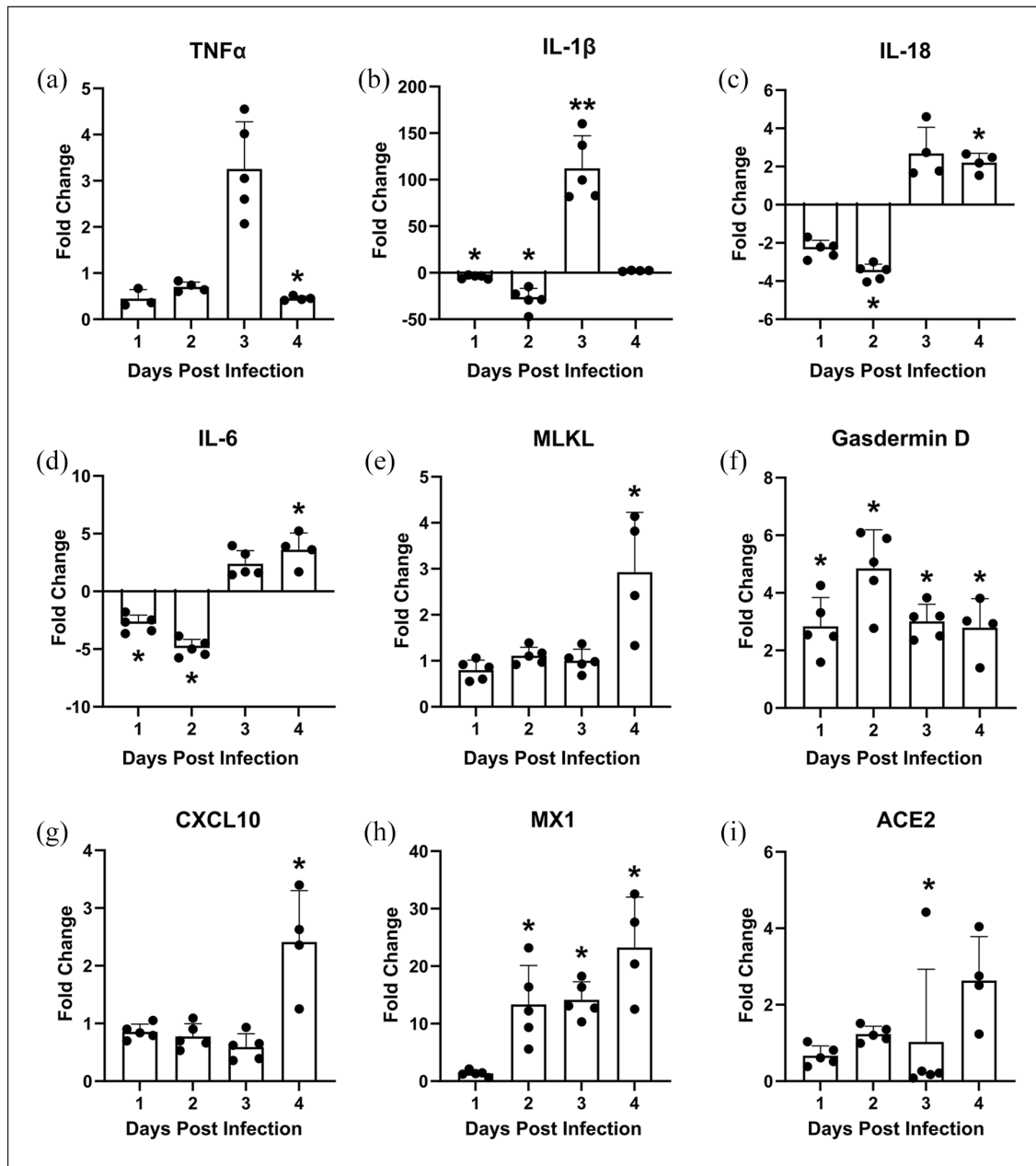


**Figure 5.** Gene expression analysis of hamster organotypic kidney cultures challenged with SARS-CoV-2. Hamster organotypic kidney cultures were cultured uninfected or infected with 1000 pfu of wild-type SARS-CoV-2 (2019-nCoV/USA\_WA/2020) and collected every day from day 1 to day 4 post-infection. In both infected and non-infected slices, gene expression was measured via RT-qPCR as the number of mRNA copies per  $\mu\text{g}$  of total RNA and normalized by the standard deviation of GAPDH expression from its average across all days. To calculate the fold changes, values from infected slices were divided by the average values of non-infected slices from the corresponding day. (a–i) Fold change in the expression of (a) TNF $\alpha$ , (b) IL-1 $\beta$ , (c) IL-18, (d) IL-6, (e) MLKL, (f) gasdermin D, (g) CXCL10, (h) MX1, (i) ACE2 from day 1 to day 4 post-infection. For each day, mRNA copy numbers per  $1 \mu\text{g}$  of RNA of infected and non-infected samples were compared using the Mann-Whitney U-test. \* =  $p < 0.05$ ; \*\* =  $p < 0.01$ .

infection kinetics observed (Figure 3(c)) with a 24-h delay. Studies in primary and immortalized human cell lines indicate that the expression of ACE2, one of the main candidate SARS-CoV-2 entry receptors, may be inducible by interferons<sup>50,51</sup> and/or IL-10.<sup>52</sup> Since the expression of numerous cytokines was delayed (or repressed) during the

first days, we also tried to follow four canonical repressive cytokines (i.e. IL-4, IL-10, IL-13, and IL-22) (Supplemental Figure S5). IL-4 and IL-22 mRNA levels remained too low to be appropriately quantified. Fold variations of IL-10 and IL-13 mRNA in infected OKCs remained lower than 2-fold compared to the non-infected ones, suggesting that

they could not be considered significant at the global organ scale. We extended our gene expression analysis to observe how infection may impact the transcription of ACE2 and other putative viral entry factors such as the receptor neuropilin-1 and the proteases TMPRSS2 and cathepsin B. A slight tendency toward the upregulation over the course of infection was detected for ACE2 (Figure 5(i)). Neuropilin-1 (Supplemental Figure S6A), TMPRSS2 (Supplemental Figure S6B), and cathepsin B (Supplemental Figure S6C) also tended toward overexpression in infected slices.

## Discussion

It remains an open question whether an active replication of SARS-CoV-2 takes place in the kidneys of COVID-19 patients with AKI. Several groups have detected the presence of a significant viral load in the kidney via methods such as RT-qPCR, in situ hybridization, immunohistochemistry, transmission electron microscopy and isolation of live virus.<sup>16,18–22,53</sup> Others have failed to find viral particles or RNA in autopsy samples,<sup>54–56</sup> thus questioning the actual replication of SARS-CoV-2 in the kidneys and the relevance of measuring viral load post-mortem, and bringing to light the heterogeneity of the samples and quantification methods used. In humans, SARS-CoV-2 infection tends to progress asymptotically or with mild symptoms before deteriorating into a severe form.<sup>3,57</sup> Therefore, only late samples which do not provide the possibility to pinpoint the starting point of renal infection are available. Recent studies showed progress on organoids obtained from human induced pluripotent stem cells,<sup>58</sup> which present the advantage of enabling work with human tissue, as we have shown elsewhere for human brain organoids and Measles virus.<sup>59</sup> However, their main limitation, apart from the impossibility to model fluid circulation, remains that such organoids still allow working only with one or two tissues at a time, which restricts the number of questions that such models can address. The absence of an appropriate model is the principal reason for the lack of knowledge on SARS-CoV-2 replication in the kidneys.<sup>7</sup> Here, we present hamster OKCs as a relevant ex vivo model for studying the infection of the kidney by SARS-CoV-2. Hamster OKCs conserved the native structure of renal tissue (Figure 1) and could be maintained in culture for at least 4 days (Figure 2). While their mitochondrial metabolic activity progressively decreased by day 4, it remained compatible with cell viability (Figure 2(a)–(c)) as confirmed by the stable quantity of RNA extracted from OKCs and their GAPDH expression pattern at later timepoints (Figure 2(d) and (e)). We further demonstrated by immunostaining that all cell types were still present after 4 days of culture, confirming that the decrease of viability was not selective for one cell type (Figure 4, Supplemental Figures S3 and S4). Hence, these cultures thus provide a relevant ex vivo culture model for studying renal infections.

SARS-CoV-2 was found in the kidneys of experimentally infected hamsters, but its ability to replicate in them was not confirmed.<sup>32</sup> In this study, organotypic kidney culture modeling showed that hamster renal tissue is highly permissive to SARS-CoV-2 infection and allows for efficient viral replication. The viral load peaked on day 1 post-infection, similarly to the dynamics observed in organotypic lung cultures but distinctly from those observed in organotypic cerebellum and brainstem cultures, where infection peaked on day 2.<sup>25</sup> To go further, we confirmed these observations in OKCs from K18-hACE2 mice, which showed very similar infection dynamics, as assessed by the production of PFUs both in tissue and culture medium (Supplemental Figure S1). We have also confirmed that the tendency of SARS-CoV-2 infection to start in the cortical area was not an artifact of the infection technique by demonstrating that the pan-tropic Vesicular Stomatitis Virus extensively infected the medullar area from day 1 post-infection (Supplemental Figures S1 and S2). Immunostainings revealed the predominant infection of CD34<sup>+</sup> endothelial cells on day 1 post-infection (Figure 4(a)). Indeed, SARS-CoV-2 infection can provoke endotheliitis in a range of organs, including the kidney. The presence of viral particles in glomerular endothelial cells in a kidney autopsy sample has also been confirmed via transmission electron microscopy.<sup>60</sup> Thus, in hamster OKCs, SARS-CoV-2 could first target endothelial cells and later disseminate to other sites, including proximal tubules (Figure 4(c)). In contrast, we did not observe any infection in podocytes. Whether hamster podocytes lack an essential viral entry or replication factor remains to be deciphered. Endothelial cells would be the first renal cells to encounter viral particles in case of viremia in a living organism and interestingly, this sequence of infection seems to be conserved in organotypic cultures.

Acute tubular injury is the most common renal pathology observed in kidney autopsy samples of COVID-19 patients.<sup>5,7,18,20,53,61</sup> Although organotypic cultures are inoculated by placing a virus-containing droplet on top of the entire slice, infection of proximal tubular epithelial cells did not occur before day 4 post-infection (Supplemental Figure S4B). This was confirmed not to be a technical artifact (Supplemental Figures S1 and S2). In contrast, they became the main infected cell population on day 4 post-infection (Figure 4(c)). This suggests that the susceptibility and permissiveness of tubular epithelia is favored by additional factors, most likely produced by the infection of other cell populations. Our results may reflect the fact that tubular damage is a late event in SARS-CoV2 pathogenesis, which makes it difficult to predict.

Despite the viral load peaking on day 1 post-infection, pro-inflammatory cytokine upregulation was not observed in hamster OKCs until day 3 for IL-1 $\beta$  (Figure 5(b)), IL-18 (Figure 5(c)), IL-6 (Figure 5(d)), and TNF $\alpha$  (Figure 5(a)) and day 4 for CXCL10 (Figure 5(g)). Moreover, a strong



repression of IL-1 $\beta$ , IL-18, and IL-6 was observed on days 1 and 2 post-infection. Such a delay in mounting a strong pro-inflammatory response may be explained by the dominance of anti-inflammatory cytokines released early in the course of the infection. Indeed, a previously described role of IL-10 secreted by infected endothelial cells,<sup>62</sup> the primary targets of SARS-CoV-2 in OKCs (Figure 4(a)), in repressing pro-inflammatory responses has to be considered here. Furthermore, resident monocyte-derived macrophages could potentially be present in high amounts in organotypic cultures and serve as a major source of IL-10 production following interaction with SARS-CoV-2.<sup>63,64</sup> As the initially infected subcapsular parietal cells die, they may relay the infection to proximal tubular epithelial cells from day 2 to day 3, where the repression of pro-inflammatory cytokines and IFN no longer occurs. Indeed, the late transcriptional upregulation of the pro-inflammatory cytokines IL-1 $\beta$ , IL-18, and IL-6 observed on day 3 post-infection (Figure 5(b)–(d)) correlated with dissemination of the virus into proximal tubular epithelial cells (Figure 4(c)). Once again, a two-step model of infection could be the result of an initial strong release of a repressor, which could dampen the expression of inflammatory cytokines at early timepoints but also promote the expression of SARS-CoV-2 receptor ACE-2 in bystander cells.<sup>52</sup> This could favor viral spreading to additional cell populations within the tissue. However, the expression of the four canonical repressive cytokines (IL-4, IL-10, IL-13, IL-22) did not vary significantly at the global culture scale (Supplemental Figure S5). Thus, further investigation via global transcriptomic analysis or single-cell approaches is required to determine what causes the delay in the pro-inflammatory cytokine response and whether specific cells are expressing IL-10 or its equivalent locally, but not in a way detectable at the organ scale. Furthermore, the virus itself could be at the origin of this repression, especially in the kidney, via a mechanism that also remains to be determined.

In parallel to pro-inflammatory cytokines, MX1 and CXCL10, two interferon-stimulated genes,<sup>65,66</sup> were induced. MX1 was only induced only on day 2 post-infection (Figure 5(h)), which could indicate a potential delay in the IFN response. Indeed, numerous SARS-CoV-2 factors were reported to interfere with innate immunity pathways, including IFN signaling.<sup>67–72</sup> Interestingly, the peak IFN response mounted by OKCs challenged with SARS-CoV-2 was significantly less pronounced in comparison to that observed in organotypic lung and brainstem cultures,<sup>25</sup> potentially supporting an important role of a repressor in viral spread or simply fewer cells capable of IFN production. Whether the relatively attenuated interferon response of the kidney contributes to pathogenesis in COVID-19 patients should be further investigated further.

While MX1 was strongly upregulated on day 2 post-infection (Figure 5(h)), CXCL10 expression did not increase markedly until day 4 (Figure 5(g)), suggesting its independence from the interferon pathway in this specific

context. However, CXCL10 can also be induced directly by IL-6. It has been reported that in the lungs SARS-CoV-2 infection leads to the overexpression of IL-6, which then stimulates CXCL10 production.<sup>73</sup> The late induction of CXCL10 may, therefore, reflect the two-step susceptibility of the model, where induction of IL-6 eventually leading to the late overexpression of CXCL10 mRNA only occurs when the infection of proximal tubular cells reaches a certain threshold.

The upregulation of MLKL (Figure 5(e)) associated with cell death via necroptosis occurred concomitantly with the increase of TNF $\alpha$  transcription on day 3 post-infection (Figure 5(a)). TNF $\alpha$  binding to tumor necrosis factor receptors (TNFR) is known to trigger necroptosis.<sup>74</sup> In addition, necroptosis can be activated via direct sensing of PAMPs by TLRs<sup>75</sup> and cytosolic nucleic acid sensors.<sup>76</sup> Day 4 post-infection is also the time where immunofluorescence staining reveals significant virus propagation into proximal tubules (Figure 4(c)). Possibly, proximal tubular epithelia are more susceptible to necroptosis due to elevated levels of TNF $\alpha$ , and its receptors compared to the initial targets of SARS-CoV-2.

Pyroptosis is another form of inflammatory programmed cell death. It is induced by inflammasome sensors responsive to activation by nuclear factor kappa B (NF- $\kappa$ B) following TLR, TNFR and interleukin-1 receptor (IL-1R) sensing.<sup>49</sup> Interestingly, while the expression of the pyroptosis mediator gasdermin D mRNA was elevated throughout the 4 days of infection in OKCs, IL-1 $\beta$  and IL-18 mRNA levels remained repressed for the first 2 days of infection before strongly increasing on day 3 post-infection (Figure 5(b), (c) and (f)). As discussed by Ferren et al.<sup>25</sup> such discrepancy may result from the involvement of another cytokine belonging to the IL-1 family. Indeed, a prolonged secretion of IL-33 following infection in OKCs could be triggering pyroptosis within the tissue through the ST2 receptor activity<sup>77</sup> for the first 2 days. Then, once SARS-CoV-2 spreads to proximal tubules on day 3 post-infection, IL-1 $\beta$  and IL-18 mRNA levels may increase and contribute to pyroptosis from this point.<sup>49</sup> Moreover, pyroptosis itself leads to the amplification of inflammation via the cleavage of cytosolic pro-IL-1 $\beta$  and pro-IL-18 into their active forms and their release from the cell.<sup>78–80</sup>

To which extent the observations made in hamster OKCs reflect SARS-CoV-2 infection of human kidneys remains to be investigated. However, OKCs offer for the first time a window on the early events of infection at the organ level. Understanding these events is essential for elucidating the pathogenesis of later stage renal dysfunction and of long-term renal sequelae alike, and provides the basis for developing adequate treatments. The poor annotation of hamster genomes and the lack of molecular biology tools adapted to hamsters begin to be inverted, allowing for a better characterization of host-pathogen interactions. The use of OKCs could be extended to studying other human nephrotropic

pathogens such as the Nipah virus, for which golden Syrian hamsters are an established model<sup>81</sup> as well as other emergent viruses including feline morbillivirus (FeMV)<sup>82,83</sup> and bat nephrotropic viruses.<sup>84</sup> Other human viruses capable of infecting the kidney include polyomavirus, cytomegalovirus, parvovirus, Epstein-Barr virus, adenovirus. Such infections are especially common in immunocompromised hosts, including renal transplant recipients and HIV-infected patients.<sup>85,86</sup> OKCs could also be of interest for early drug screening, and this will be investigated in the near future. Therefore, OKCs represents a general platform for studying kidney infections by SARS-CoV-2, that could be extended to other viruses and pathogens with a potential for drug discovery.

### Acknowledgements

We acknowledge World Reference Center for Emerging Viruses and Arboviruses (WRCEVA) and UTMB investigator, Dr. Pei Yong Shi for kindly providing recombinant icSARS-CoV-2-mNG virus based on 2019-nCoV/USA\_WA1/2020 isolate. We acknowledge the contribution of the AniRA-ImmOs metabolic phenotyping platform of the SFR Biosciences (UMS3444/CNRS, US8/Inserm, ENS de Lyon, UCBL) and we gratefully thank Laurence Canaple for technical assistance. We thank the Plateau Technique d'Imagerie/Microscopie (PLATIM) facility, where confocal microscopy experiments were conducted.





### Declaration of conflicting interests

The author(s) declared no potential conflicts of interest with respect to the research, authorship, and/or publication of this article.

### Funding

The author(s) disclosed receipt of the following financial support for the research, authorship, and/or publication of this article: The authors disclosed receipt of the following financial support for the research, authorship, and/or publication of this article: this work was supported by ANR-CoronaPepStop (ANR-20-COVI-000) and Fondation de France to BH, ANRS-COV8-SARSrhinCell to CM and CIRI-Intramural grant to LPC and CM.

### ORCID iDs

Sophie R Shyfrin  <https://orcid.org/0000-0002-5512-8664>  
 Marion Ferren  <https://orcid.org/0000-0003-4117-7411>  
 Xavier Charmetant  <https://orcid.org/0000-0002-2162-5873>  
 Cyrille Mathieu  <https://orcid.org/0000-0002-6682-2029>

### Supplemental material

Supplemental material for this article is available online.

### References

1. Zhou P, Yang X, Lou, et al. A pneumonia outbreak associated with a new coronavirus of probable bat origin. *Nature* 2020; 579: 270–273.
2. Worldometer. Coronavirus cases, <https://www.worldometers.info/coronavirus/> (2022, accessed 11 March 2022).
3. Xie J, Wu W, Li S, et al. Clinical characteristics and outcomes of critically ill patients with novel coronavirus infectious disease (COVID-19) in China: a retrospective multicenter study. *Intensive Care Med* 2020; 46: 1863–1872.
4. Chan L, Chaudhary K, Saha A, et al. AKI in hospitalized patients with COVID-19. *J Am Soc Nephrol* 2021; 32: 151–160.
5. George JA and Khoza S. SARS-CoV-2 infection and the kidneys: an evolving picture. *Adv Exp Med Biol* 2021; 1327: 107–118.
6. Hirsch JS, Ng JH, Ross DW, et al. Acute kidney injury in patients hospitalized with COVID-19. *Kidney Int* 2020; 98: 209–218.
7. Nadim MK, Forni LG, Mehta RL, et al. COVID-19-associated acute kidney injury: consensus report of the 25th Acute Disease Quality Initiative (ADQI) Workgroup. *Nat Rev Nephrol* 2020; 16: 747–764.
8. Nimkar A, Naaraayan A, Hasan A, et al. Incidence and risk factors for acute kidney injury and its effect on mortality in patients hospitalized from COVID-19. *Mayo Clin Proc Innov Qual Outcomes* 2020; 4: 687–695.
9. Svetitsky S, Shuaib R, McAdoo S, et al. Long-term effects of Covid-19 on the kidney. *QJM An Int J Med* 2021; 114: 621–622.
10. Fisher M, Neugarten J, Bellin E, et al. AKI in hospitalized patients with and without COVID-19: a comparison study. *J Am Soc Nephrol* 2020; 31: 2145–2157.
11. Huang C, Huang L, Wang Y, et al. 6-month consequences of COVID-19 in patients discharged from hospital: a cohort study. *Lancet* 2021; 397: 220–232.
12. Al-Aly Z, Xie Y and Bowe B. High-dimensional characterization of post-acute sequelae of COVID-19. *Nature* 2021; 594: 259–264.
13. Wu L, Wu Y, Xiong H, et al. Persistence of symptoms after discharge of patients hospitalized due to COVID-19. *Front Med* 2021; 8: 761314.
14. Copur S, Berkkan M, Basile C, et al. Post-acute COVID-19 syndrome and kidney diseases: what do we know? *J Nephrol* 2022; 35: 795–805.
15. Khan S, Chen L, Yang CR, et al. Does SARS-cov-2 infect the kidney? *J Am Soc Nephrol* 2020; 31: 2746–2748.
16. Braun F, Lütgehetmann M, Pfefferle S, et al. SARS-CoV-2 renal tropism associates with acute kidney injury. *Lancet* 2020; 396: 597–598.
17. Brienza N, Puntillo F, Romagnoli S, et al. Acute kidney injury in Coronavirus disease 2019 infected patients: a meta-analytic study. *Blood Purif* 2021; 50(1): 35–41.
18. Diao B, Wang C, Wang R, et al. Human kidney is a target for novel severe acute respiratory syndrome coronavirus 2 infection. *Nat Commun* 2021; 12: 2506.
19. Puelles VG, Lütgehetmann M, Lindenmeyer MT, et al. Multiorgan and renal tropism of SARS-CoV-2. *N Engl J Med* 2020; 383: 590–592.
20. Su H, Yang M, Wan C, et al. Renal histopathological analysis of 26 postmortem findings of patients with COVID-19 in China. *Kidney Int* 2020; 98: 219–227.
21. Hanley B, Naresh KN, Roufosse C, et al. Histopathological findings and viral tropism in UK patients with severe fatal

- COVID-19: a post-mortem study. *Lancet Microbe* 2020; 1: e245–e253.
22. Liu J, Li Y, Liu Q, et al. SARS-CoV-2 cell tropism and multiorgan infection. *Cell Discov* 2021; 7: 17.
  23. Alpers CE and Kowalewska J. Emerging Paradigms in the renal pathology of viral diseases. *Clin J Am Soc Nephrol* 2007; 2: S6–S12.
  24. Prasad N and Patel MR. Infection-induced kidney diseases. *Front Med* 2018; 5: 327.
  25. Ferren M, Favède V, Decimo D, et al. Hamster organotypic modeling of SARS-CoV-2 lung and brainstem infection. *Nat Commun* 2021; 12(1): 5809.
  26. Welsch JC, Charvet B, Dussurgey S, et al. Type I interferon receptor signaling drives selective permissiveness of astrocytes and microglia to measles virus during brain infection. *J Virol* 2019; 93: e00618–19.
  27. Bloyet L-M, Welsch J, Enchery F, et al. HSP90 chaperoning in addition to phosphoprotein required for folding but not for supporting enzymatic activities of measles and Nipah virus L polymerases. *J Virol* 2016; 90: 6642–6656.
  28. Poosti F, Pham BT, Oosterhuis D, et al. Precision-cut kidney slices (PCKS) to study development of renal fibrosis and efficacy of drug targeting ex vivo. *Dis Model Mech* 2015; 8: 1227–1236.
  29. Genovese F, Kárpáti ZS, Nielsen SH, et al. Precision-Cut kidney slices as a tool to understand the dynamics of extracellular matrix remodeling in renal fibrosis. *Biomark Insights* 2016; 11: 77–84.
  30. Zhang S, Liu Q, Xiao J, et al. Molecular validation of the precision-cut kidney slice (PCKS) model of renal fibrosis through assessment of TGF- $\beta$ 1-induced Smad and p38/ERK signaling. *Int Immunopharmacol* 2016; 34: 32–36.
  31. Bigaeva E, Puerta Cavanzo N, Stribos EGD, et al. Predictive value of Precision-Cut kidney slices as an ex vivo screening platform for therapeutics in human renal fibrosis. *Pharmaceutics* 2020; 12: 459.
  32. Chan JFW, Zhang AJ, Yuan S, et al. Simulation of the clinical and pathological manifestations of Coronavirus disease 2019 (COVID-19) in a Golden Syrian hamster model: implications for disease pathogenesis and transmissibility. *Clin Infect Dis* 2020; 71: 2428–2446.
  33. Welsch J, Lionnet C, Terzian C, et al. Organotypic brain cultures: a framework for studying CNS infection by neurotropic viruses and screening antiviral drugs. *Bio Protoc* 2017; 7: e2605.
  34. Xie X, Muruato A, Lokugamage KG, et al. An infectious cDNA clone of SARS-CoV-2. *Cell Host Microbe* 2020; 27: 841–848.e3.
  35. Underwood E, Redell JB, Zhao J, et al. A method for assessing tissue respiration in anatomically defined brain regions. *Sci Rep* 2020; 10: 13179.
  36. Pfaffl MW. A new mathematical model for relative quantification in real-time RT-PCR. *Nucleic Acids Res* 2001; 29: e45.
  37. Mathieu C, Pohl C, Szecsi J, et al. Nipah virus uses leukocytes for efficient dissemination within a host. *J Virol* 2011; 85: 7863–7871.
  38. Preibisch S, Saalfeld S and Tomancak P. Globally optimal stitching of tiled 3D microscopic image acquisitions. *Bioinformatics* 2009; 25: 1463–1465.
  39. Schneider CA, Rasband WS and Eliceiri KW. NIH image to ImageJ: 25 years of image analysis. *Nat Methods* 2012; 9: 671–675.
  40. GraphPad. GraphPad Software, www.graphpad.com (2021).
  41. Kurts C, Panzer U, Anders HJ, et al. The immune system and kidney disease: Basic concepts and clinical implications. *Nat Rev Immunol* 2013; 13: 738–753.
  42. Hoffmann M, Kleine-Weber H, Schroeder S, et al. SARS-CoV-2 cell entry depends on ACE2 and TMPRSS2 and is blocked by a clinically proven protease inhibitor. *Cell* 2020; 181: 271–280.e8.
  43. Ou X, Liu Y, Lei X, et al. Characterization of spike glycoprotein of SARS-CoV-2 on virus entry and its immune cross-reactivity with SARS-CoV. *Nat Commun* 2020; 11: 1620.
  44. Uhlén M, Fagerberg L, Hallström BM, et al. Tissue-based map of the human proteome. *Science* 2015; 347: 1260419.
  45. Gkogkou E, Barnasas G, Vougas K, et al. Expression profiling meta-analysis of ACE2 and TMPRSS2, the putative anti-inflammatory receptor and priming protease of SARS-CoV-2 in human cells, and identification of putative modulators. *Redox Biol* 2020; 36: 101615.
  46. Paul M, Poyan Mehr A and Kreutz R. Physiology of local renin-angiotensin systems. *Physiol Rev* 2006; 86: 747–803.
  47. Bertheloot D, Latz E and Franklin BS. Necroptosis, pyroptosis and apoptosis: an intricate game of cell death. *Cell Mol Immunol* 2021; 18: 1106–1121.
  48. Christofferson DE and Yuan J. Necroptosis as an alternative form of programmed cell death. *Curr Opin Cell Biol* 2010; 22: 263–268.
  49. Bergsbaken T, Fink SL and Cookson BT. Pyroptosis: host cell death and inflammation. *Nat Rev Microbiol* 2009; 7: 99–109.
  50. Busnadiego I, Fernbach S, Pohl MO, et al. Antiviral activity of type i, ii, and iii interferons counterbalances ace2 inducibility and restricts sars-cov-2. *mBio* 2020; 11: 1–10.
  51. Ziegler CGK, Allon SJ, Nyquist SK, et al. SARS-CoV-2 receptor ACE2 is an interferon-stimulated gene in human airway epithelial cells and is detected in specific cell subsets across tissues. *Cell* 2020; 181: 1016–1035.e19.
  52. Albin A, Calabrone L, Carlini V, et al. Preliminary evidence for IL-10-Induced ACE2 mRNA expression in lung-derived and endothelial cells: implications for SARS-Cov-2 ARDS pathogenesis. *Front Immunol* 2021; 12: 718136.
  53. Farkash EA, Wilson AM and Jentzen JM. Ultrastructural evidence for direct renal infection with SARS-CoV-2. *J Am Soc Nephrol* 2020; 31: 1683–1687.
  54. Gaillard F, Ismael S, Sannier A, et al. Tubuloreticular inclusions in COVID-19-related collapsing glomerulopathy. *Kidney Int* 2020; 98: 241.
  55. Peleg Y, Kudose S, D'Agati V, et al. Acute kidney injury due to collapsing glomerulopathy following COVID-19 infection. *Kidney Int Rep* 2020; 5: 940–945.
  56. Santoriello D, Khairallah P, Bombardieri AS, et al. Postmortem kidney pathology findings in patients with COVID-19. *J Am Soc Nephrol* 2020; 31: 2158–2167.

57. Wang Y, Wang Y, Chen Y, et al. Unique epidemiological and clinical features of the emerging 2019 novel coronavirus pneumonia (COVID-19) implicate special control measures. *J Med Virol* 2020; 92: 568–576.
58. Monteil V, Kwon H, Prado P, et al. Inhibition of SARS-CoV-2 infections in engineered human tissues using clinical-grade soluble human ACE2. *Cell* 2020; 181: 905–913.e7.
59. Mathieu C, Bovier FT, Ferren M, et al. Molecular features of the measles virus viral fusion complex that favor infection and spread in the brain. *mBio* 2021; 12(3): e0079921.
60. Varga Z, Flammer AJ, Steiger P, et al. Endothelial cell infection and endotheliitis in COVID-19. *Lancet* 2020; 395: 1417–1418.
61. Bouquegneau A, Erpicum P, Grosch S, et al. COVID-19-associated nephropathy includes tubular necrosis and capillary congestion, with evidence of SARS-CoV-2 in the nephron. *Kidney360* 2021; 2: 639–652.
62. Azizan A, Sweat J, Espino C, et al. Differential proinflammatory and angiogenesis-specific cytokine production in human pulmonary endothelial cells, HPMEC-ST1.6R infected with dengue-2 and dengue-3 virus. *J Virol Methods* 2006; 138: 211–217.
63. Daviaud N, Garbayo E, Schiller PC, et al. Organotypic cultures as tools for optimizing central nervous system cell therapies. *Exp Neurol* 2013; 248: 429–440.
64. Islam H, Chamberlain TC, Mui AL, et al. Elevated interleukin-10 levels in COVID-19: potentiation of pro-inflammatory responses or impaired anti-inflammatory action? *Front Immunol* 2021; 12: 677008.
65. Haller O, Staeheli P and Kochs G. Interferon-induced Mx proteins in antiviral host defense. *Biochimie* 2007; 89: 812–818.
66. Majumder S, Zhou LZ, Chaturvedi P, et al. P48/STAT1alpha-containing complexes play a predominant role in induction of IFN-gamma-inducible protein, 10 kDa (IP-10) by IFN-gamma alone or in synergy with TNF-alpha. *J Immunol* 1998; 161: 4736–4744.
67. Perrin-Cocon L, Diaz O, Jacquemin C, et al. The current landscape of coronavirus-host protein-protein interactions. *J Transl Med* 2020; 18: 319.
68. Sa Ribero M, Jouvenet N, Dreux M, et al. Interplay between SARS-CoV-2 and the type I interferon response. *PLoS Pathog* 2020; 16: e1008737.
69. Pawlica P, Yario TA, White S, et al. SARS-CoV-2 expresses a microRNA-like small RNA able to selectively repress host genes. *Proc Natl Acad Sci U S A* 2021; 118: e2116668118.
70. Wu J, Shi Y, Pan X, et al. SARS-cov-2 ORF9b inhibits RIG-I-MAVS antiviral signaling by interrupting k63-linked ubiquitination of NEMO. *Cell Rep* 2021; 34: 108761.
71. Chen K, Xiao F, Hu D, et al. SARS-CoV-2 nucleocapsid protein interacts with RIG-I and represses RIG-Mediated IFN- $\beta$  production. *Viruses* 2020; 13: E47.
72. Mu J, Fang Y, Yang Q, et al. SARS-CoV-2 N protein antagonizes type I interferon signaling by suppressing phosphorylation and nuclear translocation of STAT1 and STAT2. *Cell Discov* 2020; 6: 65.
73. Coperchini F, Chiovato L and Rotondi M. Interleukin-6, CXCL10 and infiltrating macrophages in COVID-19-related cytokine storm: not one for all but all for one! *Front Immunol* 2021; 12: 668507.
74. Holler N, Zaru R, Micheau O, et al. Fas triggers an alternative, caspase-8-independent cell death pathway using the kinase RIP as effector molecule. *Nat Immunol* 2000; 1: 489–495.
75. He S, Liang Y, Shao F, et al. Toll-like receptors activate programmed necrosis in macrophages through a receptor-interacting kinase-3-mediated pathway. *Proc Natl Acad Sci U S A* 2011; 108: 20054–20059.
76. Schock SN, Chandra NV, Sun Y, et al. Induction of necroptotic cell death by viral activation of the RIG-I or STING pathway. *Cell Death Differ* 2017; 24: 615–625.
77. Cohen ES, Scott IC, Majithiya JB, et al. Oxidation of the alarmin IL-33 regulates ST2-dependent inflammation. *Nat Commun* 2015; 6: 1–10.
78. Baroja-Mazo A, Martín-Sánchez F, Gomez AI, et al. The NLRP3 inflammasome is released as a particulate danger signal that amplifies the inflammatory response. *Nat Immunol* 2014; 15: 738–748.
79. Kanneganti TD, Body-Malapel M, Amer A, et al. Critical role for cryopyrin/nalp3 in activation of caspase-1 in response to viral infection and double-stranded RNA. *J Biol Chem* 2006; 281: 36560–36568.
80. Wang K, Sun Q, Zhong X, et al. Structural Mechanism for GSDMD targeting by autoprocessed caspases in pyroptosis. *Cell* 2020; 180: 941–955.e20.
81. Wong KT, Grosjean I, Brisson C, et al. A golden hamster model for Human Acute Nipah virus infection. *Am J Pathol* 2003; 163: 2127–2137.
82. Choi EJ, Ortega V and Aguilar HC. Feline Morbillivirus, a new paramyxovirus possibly associated with feline kidney disease. *Viruses* 2020; 12: E501.
83. De Luca E, Sautto GA, Crisi PE, et al. Feline Morbillivirus infection in domestic cats: what have we learned so far? *Viruses* 2021; 13: 683.
84. de Souza WM, Fumagalli MJ, Carrera JP, et al. Paramyxoviruses from neotropical bats suggest a novel genus and nephrotropism. *Infect Genet Evol* 2021; 95: 105041.
85. Mikulak J and Singhal PC. HIV-1 and kidney cells: better understanding of viral interaction. *Nephron Exp Nephrol* 2010; 115: e15–e21.
86. Singh HK and Nickleleit V. Kidney disease caused by viral infections. *Curr Diagn Pathol* 2004; 10: 11–21.